Quaternion-based Signal Processing

Ben Witten and Jeff Shragge, Stanford University*

SUMMARY

Hypercomlex numbers are primarily used for pattern recognition, offer many useful applications to geophysics. Image disparity estimation is a hypercomplex, phase-based technique, using quaternions that can find differences between subtly varying images. This technique relies on applying a quaternionic Fourier transform, a quaternionic Gabor filter and exploits the symmetries inherent in the quaternion. Two applications of hypercomplex image disparity estimation examined here are time lapse analysis and boundary detection.

INTRODUCTION

Hypercomplex numbers are multi-dimensional numbers that have more than one complex plane. The most common type of hypercomplex numbers have one real and three complex dimensions. These were introduced by Hamilton (1866) who termed them quaternions. The most common application of quaternions has been towards Maxwell's equations. Recently, however, quaternions have been applied to signal processing, most notably pattern recognition. They are useful for color image analysis where previous techniques have failed because each complex quaternion axis can be associated with an RGB axis (Sanwine and Ell, 2000) which allows for color edge detection. In addition, they can be used for image segmentation, finding structure based not only upon color, but repeating patters. This has proven useful for finding defects in textiles (Bülow and Sommer, 2001). Another application is image disparity, which is used by Bülow (1999) to show how a pattern changes between two frames of a movie.

Image disparity techniques offer many geophysical applications because only organized structures and patterns are detected by image disparity. Thus, noise will have minimal effect. Since it is a phase based technique, even low amplitude signal still retain enough information to be viable for image disparity estimation. The applications that will be discussed here are time lapse analysis and edge detection. To this end we show the basics of hypercomplex mathematics define the the quaternionic Fourier transform. We then define the Gabor filter and extend it to the quaternionic case. This will allow for the image disparity estimation to be calculated based upon multiple complex phases.

HYPERCOMPLEX MATHEMATICS

The set of hypercomplex numbers is defined as

$$q = q_0 + \sum_{l=1}^{n} i_l q_l, \quad q_l \in \Re. \tag{1}$$

Hypercomplex numbers define a n+1-dimensional complex space with i_l orthonormal to i_m, for $l \neq m$. For all cases presented in this paper l will be limited to 3. Such numbers are quaternions, which can be represented as $q = q_0 + iq_1 + jq_2 + kq_3$, where i, j, k are imaginary numbers that satisfying the following relations:

$$ij = -ji = k, \quad \text{and} \quad \mathrm{i}^2 = \mathrm{j}^2 = \mathrm{k}^2 = -1. \tag{2}$$

The multiplication table for quaternion unit vectors is shown in Table 1. With these definitions, quaternionic addition between two quaternions, q and p, can be defined as

$$\begin{aligned} q + p &= (q_0 + iq_1 + jq_2 + kq_3) + (p_0 + ip_1 + jp_2 + kp_3) \\ &= (q_0 + p_0) + i(q_1 + p_1) + j(q_2 + p_2) + k(q_3 + p_3), \end{aligned} \tag{3}$$

and multiplication as

$$\begin{aligned} qp &= (q_0 + iq_1 + jq_2 + kq_3)(p_0 + ip_1 + jp_2 + kp_3) \\ &= (q_0 p_0 - q_1 p_1 - q_2 p_2 - q_3 p_3) \\ &\quad + i(q_0 p_1 + q_1 p_0 + q_2 p_3 - q_3 p_2) \\ &\quad + j(q_0 p_2 + q_2 p_0 - q_1 p_3 + q_3 p_1) \\ &\quad + k(q_0 p_3 + q_3 p_0 + q_1 p_2 - q_2 p_1). \end{aligned} \tag{4}$$

Table 1: The multiplication table for quaternion algebra.

	1	i	j	k
1	1	i	j	k
i	i	-1	k	$-j$
j	j	$-k$	-1	i
k	k	j	$-i$	-1

Notice that multiplication in equation 4 is not commutative due to the quaternionic algebra rules defined in table 1. Quaternions are often separated into two parts, q_0 and $\mathbf{q} = iq_1 + jq_2 + kq_3$, respectively called the scalar and vector part of the quaternion. Using this definition, the conjugate of q, $\bar{q}$, is

$$\bar{q} = q_0 - \mathbf{q} = q_0 - iq_1 - jq_2 - kq_3 \tag{5}$$

and the norm of a quaternion is defined by

$$|| \, q \, || = \sqrt{q\bar{q}} = \sqrt{{q_0}^2 + {q_1}^2 + {q_2}^2 + {q_3}^2}. \tag{6}$$

It is useful to formulate a polar representation of the quaternion, with phase and modulus. For any complex number, $\mathbf{z} = a + ib$, the argument or phase-angle is defined as atan2(b,a). If $\mathbf{z}$ is written it the form $\mathbf{z} = | \, r \, | \, e^{i\gamma}$, then γ is the phase (argument) of $\mathbf{z}$, denoted arg($\mathbf{z}$)=γ. Quaternions contain three complex subfields and, correspondingly, three phases components which are:

$$\phi = \text{atan2}(\mathrm{n}_\phi, \mathrm{d}_\phi), \tag{7}$$

$$\theta = \text{atan2}(\mathrm{n}_\theta, \mathrm{d}_\theta), \tag{8}$$

$$\psi = \arcsin(\mathrm{n}_\psi), \tag{9}$$

where $n_\phi, d_\phi, n_\theta, d_\theta, n_\psi$ come from the equivalence of two homomorphic quaternion transformations and are defined as

$$n_\phi = 2(q_2 * q_3 + q_0 * q_1), \tag{10}$$

$$d_\phi = (q_0)^2 - (q_1)^2 + (q_2)^2 - (q_3)^2, \tag{11}$$

$$n_\theta = 2(q_1 * q_3 + q_0 * q_2), \tag{12}$$

$$d_\theta = (q_0)^2 + (q_1)^2 - (q_2)^2 - (q_3)^2, \tag{13}$$

$$n_\psi = 2(q_1 * q_2 + q_0 * q_3). \tag{14}$$

Quaternionic Transform

Analogous to complex numbers, quaternions can be represented by a magnitude and three phases with

$$q = || \, q \, || \, e^{i\phi} e^{j\theta} e^{k\psi}. \tag{15}$$

ψ will be considered to be 0 since only 2-D images are discussed in this paper.

Ell (1992) introduced the quaternionic Fourier transform (QFT) for two-dimensional signals,

$$F^q(\mathbf{u}) = \int_{R^2} e^{-i2\pi ux} f(\mathbf{x}) e^{-j2\pi vy} d^2\mathbf{x}, \tag{16}$$

where $\mathbf{x} = (x,y)^T$ and $\mathbf{u} = (u,v)^T \in R^2$ and f is a two-dimensional quaternion signal. Because two-dimensional signals can be decomposed into even and odd components along either the x- or y-axis, f can be written

$$f = f_{ee} + f_{oe} + f_{eo} + f_{oo},$$

with, for example, f_{oe} denoting the part of f that is odd with respect to x and even with respect to y. The QFT can now be decomposed to

$$\begin{aligned} F^q(\mathbf{u}) = & \int_{R^2} cos(2\pi ux)cos(2\pi vy) f(\mathbf{x}) d^2\mathbf{x} \\ & -i \int_{R^2} sin(2\pi ux)cos(2\pi vy) f(\mathbf{x}) d^2\mathbf{x} \\ & -j \int_{R^2} cos(2\pi ux)sin(2\pi vy) f(\mathbf{x}) d^2\mathbf{x} \\ & +k \int_{R^2} sin(2\pi ux)sin(2\pi vy) f(\mathbf{x}) d^2\mathbf{x}. \end{aligned} \tag{17}$$

The QFT is an invertible transform and most standard Fourier theorems hold for QFTs with minimal variation. These theorems will not be re-derived here, as complete proofs of the QFT extension of Rayleigh's, the shift, the modulation, the derivative, and the convolution theorem exist elsewhere (Ell, 1992; Bülow, 1999).

QUATERNIONIC GABOR FILTERS

The three different types of signal phase, as described by Bülow (1999) are global, instantaneous, and local. Global phase is the angular phase of the complex Fourier transform of a signal. It gives a real-valued number for each point in the frequency domain that is indicative of the relative position of the frequency components. Instead of giving the phase of a certain frequency component, instantaneous and local phase give the phase at a certain position in a real signal. The instantaneous and local phases, however, do this in different ways. The instantaneous phase is the angular phase of the complex value at each signal position. The instantaneous phase has the drawback that while it provides local information, that information depends on the entire signal. This causes the instantaneous phase at any point to be affected by changes at any other point in the image, regardless of separation distance. To overcome this problem, quadrature filters are employed. The local phase is defined as angular phase of the quadrature filter response at a particular position of the signal. In this paper, in order to obtain a local quaternion phase, quaternionic Gabor filters are used. While quaternionic Gabor filters are not exact quaternionic quadrature filters, they are a good approximation to them.

Gabor filters are linear time-invariant (LTI) filters that exhibit many useful properties, which have led to their use in a wide range of signal processing applications. The impulse response of a two-dimensional Gabor filter is

$$h(x,y;u_0,v_0,\sigma,\epsilon) = g(x,y;\sigma,\epsilon) e^{i2\pi(u_0 x + v_0 y)} \tag{18}$$

where $g(x,y;\sigma)$ is the Gaussian with aspect ratio ϵ,

$$g(x,y;\sigma,\epsilon) = e^{-\frac{x^2+(\epsilon y)^2}{\sigma^2}}. \tag{19}$$

Analogous to equation 18, a quaternionic Gabor filter is defined such that the impulse response to the filter is,

$$\begin{aligned} h^q(x,y;u_0,v_0,\sigma,\epsilon) &= g(x,y;\sigma,\epsilon) e^{i2\pi u_0 x} e^{j2\pi v_0 y} \\ &= g(x,y;\sigma,\epsilon) e^{i\omega_1 x} e^{j\omega_2 y} \end{aligned} \tag{20}$$

where $g(x,y;\sigma,\epsilon)$ is defined as in equation 19. The quaternionic Gabor filter can be split into its even and odd symmetries, just as the QFT and the original image. In that case the filter h can be written as

$$h^q(x,y;u_0,v_0,\sigma,\epsilon) = (h^q_{ee} + ih^q_{oe} + jh^q_{eo} + kh^q_{oo}). \tag{21}$$

Note that h^q_{ee}, h^q_{oe}, h^q_{eo}, and h^q_{oo} are real-valued functions (see Figure 1).

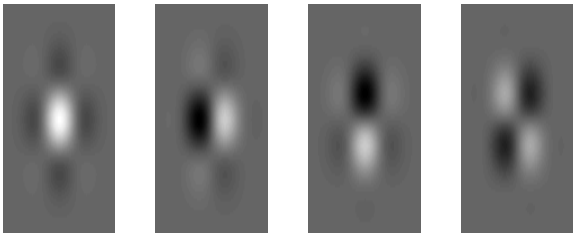

Figure 1: The h_{ee}, h_{oe}, h_{eo}, and h_{oo} symmetries of a quaternionic Gabor filter

QUATERNIONIC DISPARITY ESTIMATION

Given two images, f_1 and f_2, it is possible to find a vector field, $\mathbf{d}(d_x,d_y)$, that relates the local displacement between f_1 and f_2 (i.e. $f_1(\mathbf{x}) = f_2(\mathbf{x}+\mathbf{d}(\mathbf{x}))$. Therefore, if the QFT of f_1 is,

$$f_1(x,y) \Longrightarrow F^q(u,v), \tag{22}$$

then by the shift theorem,

$$f_2(x,y) = f_1(x+d_x, y+d_y) \Longrightarrow e^{i2\pi ud_x} F^q(u,v) e^{j2\pi ud_y}. \tag{23}$$

Knowing that f_1 and f_2 have local quaternionic phases (ϕ_1,θ_1,ψ_1) and (ϕ_2,θ_2,ψ_2) and assuming that ϕ varies only in x and θ varies only in y, then the displacement $\mathbf{d}(\mathbf{x})$ is given by

$$d_x(\mathbf{x}) = \frac{\phi_2(\mathbf{x}) - \phi_1(\mathbf{x})}{u_{ref}} \tag{24}$$

$$d_y(\mathbf{x}) = \frac{\theta_2(\mathbf{x}) - \theta_1(\mathbf{x})}{v_{ref}}. \tag{25}$$

The accuracy of the displacement depends strongly on the choice of the reference frequencies, u_{ref} and v_{ref}. The local model approach for quaternions outlined by Bülow (1999) will be used. This model assumes that the local phase at corresponding points of the two images will not differ, $\Omega_1(x,y)$=$\Omega_2(x+d_x, y+d_y)$, where Ω=(ϕ,θ). An estimate for $\mathbf{d}$ is obtained by a first-order Taylor expansion of Ω about x

$$\Omega_2(\mathbf{x}+\mathbf{d}) \approx \Omega_2(\mathbf{x}) + (\mathbf{d}\cdot\nabla)\Omega_2(\mathbf{x}). \tag{26}$$

Solving for $\mathbf{d}$ in equation 26 gives the disparity estimate for the local model. The disparity is estimated using equation 24 and the reference frequencies given by,

$$u_{ref} = \frac{\partial\phi_1}{\partial x}(\mathbf{x}), \quad v_{ref} = \frac{\partial\theta_1}{\partial y}(\mathbf{y}). \tag{27}$$

The local quaternionic phase components for anywhere in an image are given by

$$\phi(\mathbf{x}) = \frac{\text{atan2}(\text{n}_\phi(\mathbf{x}), \text{d}_\phi(\mathbf{x}))}{2}, \tag{28}$$

$$\theta(\mathbf{x}) = \frac{\text{atan2}(\text{n}_\theta(\mathbf{x}), \text{d}_\theta(\mathbf{x}))}{2}, \tag{29}$$

where n and d are related to the rotation matrix of a quaternion and are,

$$n_\phi = -2(k^q_{eo}(\mathbf{x})k^q_{oo}(\mathbf{x}) + k^q_{ee}(\mathbf{x})k^q_{oe}(\mathbf{x})), \tag{30}$$

$$d_\phi = (k^q_{ee}(\mathbf{x}))^2 - (k^q_{oe}(\mathbf{x}))^2 + (k^q_{eo}(\mathbf{x}))^2 - (k^q_{oo}(\mathbf{x}))^2, \tag{31}$$

$$n_\theta = -2(k^q_{oe}(\mathbf{x})k^q_{oo}(\mathbf{x}) + k^q_{ee}(\mathbf{x})k^q_{eo}(\mathbf{x})), \tag{32}$$

$$d_\theta = (k^q_{ee}(\mathbf{x}))^2 + (k^q_{oe}(\mathbf{x}))^2 - (k^q_{eo}(\mathbf{x}))^2 - (k^q_{oo}(\mathbf{x}))^2. \tag{33}$$

The k-functions are the responses of a symmetric component of the quaternionic Gabor filter to the image (e.g. k_{ee}=$(h_{ee} * f)(\mathbf{x})$). From equations 28 and 29 the derivatives of the local phase components are computed

$$\frac{\partial}{\partial x}\phi(\mathbf{x}) = \frac{d_\phi(\mathbf{x})\frac{\partial}{\partial x}n_\phi(\mathbf{x}) - n_\phi(\mathbf{x})\frac{\partial}{\partial x}d_\phi(\mathbf{x})}{n^2_\phi(\mathbf{x}) + d^2_\phi(\mathbf{x})}, \tag{34}$$

$$\frac{\partial}{\partial y}\theta(\mathbf{x}) = \frac{d_\theta(\mathbf{x})\frac{\partial}{\partial y}n_\theta(\mathbf{x}) - n_\theta(\mathbf{x})\frac{\partial}{\partial y}d_\theta(\mathbf{x})}{n^2_\theta(\mathbf{x}) + d^2_\theta(\mathbf{x})}. \tag{35}$$

Therefore, the disparity depends on the rate of change of the local phase as approximated by the quaternionic Gabor filters.

Figure 2 shows an instructive example with a shifted rectangular block. The upper left panel is the original block position while the upper right panel shows the same block shifted down and to the right by four points. On the bottom, the disparity is shown as both a magnitude and vector plot of the shift.

APPLICATIONS

Time Lapse

One application for this procedure is assessing the temporal variation of time-lapse images. When seismic data are acquired in the same location at different times, disparity estimation can be used to visualize changes in the subsurface caused by compaction or fluid flow. This was done with three migrated images from the Duri Field in Indonesia that were collected over a 20 month period. The original images (Lumley, 1995) are shown in figure 3 with the magnitude of the disparity between the images. The magnitude of the disparity offers very little information for this application. The vector representation, displayed in figure 4 with each vector scaled by 2, however, better accentuates the change providing useful information. Although it is hard to distinguish by looking at the migrated images, there are subtle changes that can be seen. The left edge of the hump near the center of the image increases slope from the left panel of figure 3 to the right. This slight change is detected by the image disparity algorithm and can be seen with downward pointing arrows near that have been circled in figure 4, corresponding to the left slope of the hump. This may be related to the insertion of an observation well near that location. The arrows do distinguish changes throughout the image, but it is very difficult to tell if these correspond to real changes, noise, or some slight variation caused by a change in acquisition. Figure 5 shows the original slice (time 0) overlain with the vector change between it the final time.

Edge Detection

This procedure can also be used as an automated edge detection

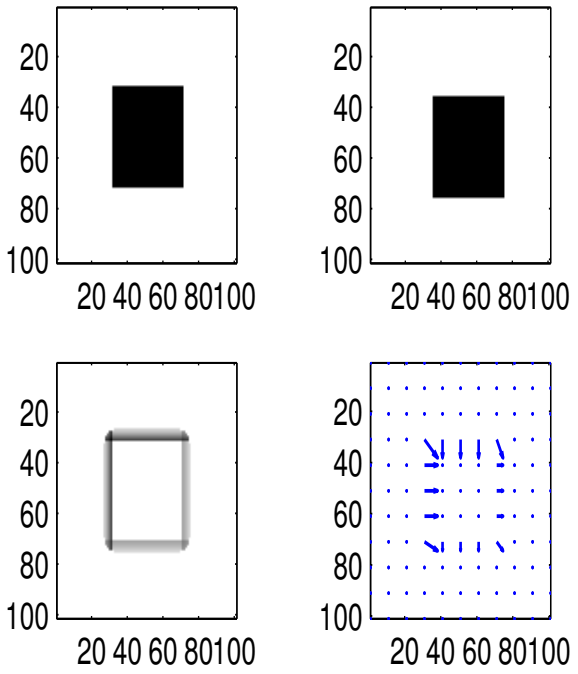

Figure 2: Top row: the input images. Bottom row: The disparity as a magnitude and a vector representation of disparity

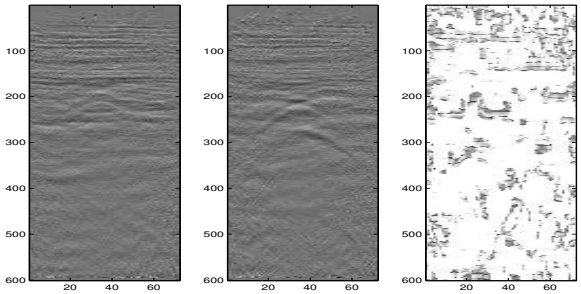

Figure 3: Two images from the same location at Duri Field at different times. Left:The magnitude of the change relative to the first image.

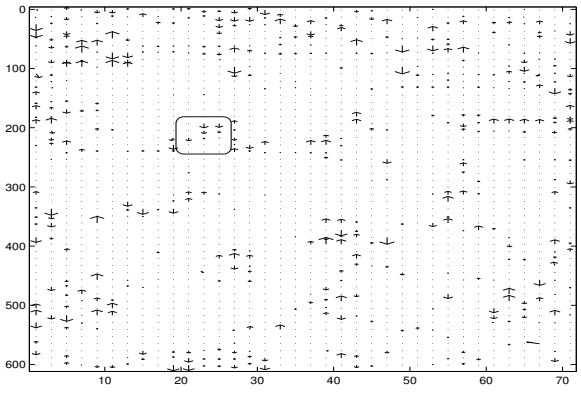

Figure 4: The disparity as a vector plot, sub-sampled by 2 in the x direction and 12 in the y direction.

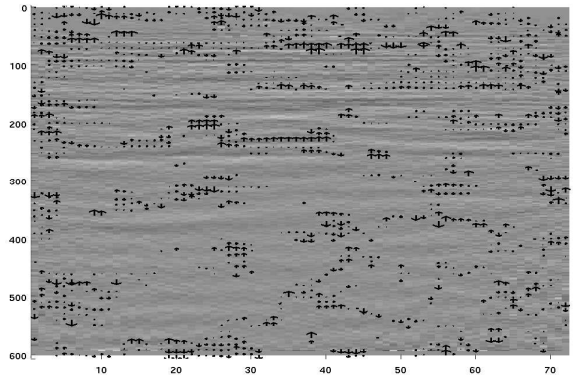

Figure 5: The original image from Duri field with how the subsurface changed overlaid on it.

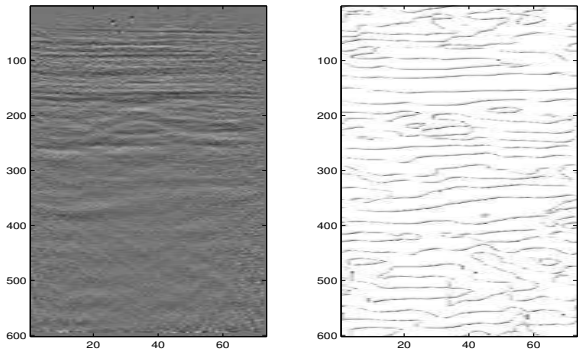

Figure 6: The original image and the boundaries found by image disparity with itself.

algorithm. This application can be accomplished by comparing a single image with a slightly shifted version of itself. When this is done the coherent structure is illuminated in the magnitude display of the disparity. Figure 6 shows the boundaries that have been detected using this algorithm for the first Duri image in figure 3. This method was also tested on a more complicated migrated data set that contains steeply dipping reflectors, from Tang and Clapp (2006) (see figure 7). The leftmost image is a gained version of the center image. The edge detection, shown on the right, was done with the ungained image (center panel). Notice that the boundaries that are not visible were still detected because of the phase-based nature of the technique. It is encouraging that even though this method fails to distinguish all of the layer boundaries that are clearly seen at the top of the original image. Although not demonstrated here, it is possible to shift only in the x-direction to highlight the vertical edges or shift in the y-direction to accentuate the horizontal edges. The sum of these two shifts will yield the same result as a single diagonal shift as done for these examples.

CONCLUSION

Hypercomplex methods in general, and quaternionic in particular, offer numerous and diverse possibilities for geophysical purposes. This method is easy to implement and efficient for time lapse analysis and boundary detection. Although the edge detection application does a reasonable job, it has not been as effective for shallow features as expected. The time lapse analysis offers an innovative way to quantitatively evaluated changes over time. In future works, this technique my be extended to three dimensional problems or

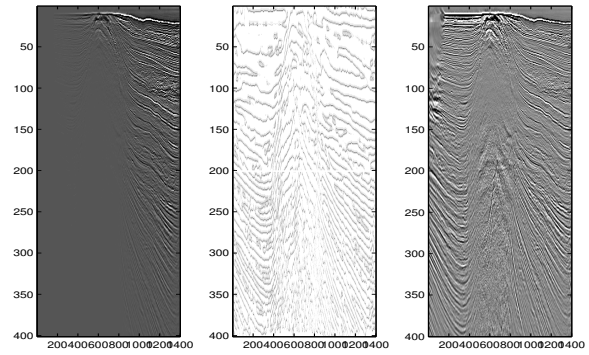

Figure 7: Edge detection example. Left: Original image. Center: The boundaries found from the original image using disparity estimation with itself. Right: A gained version of the original image.

applied to other applications such as velocity analysis.

REFERENCES

Bülow, T. and G. Sommer, 2001, Hypercomplex signals: A novel extension of the analytic signal to the multidimensional case: IEEE Transactions on Signal Processing, **49**, 2844–2852.

Bülow, T., 1999, Hyercomplex spectral signal representations fro the processing and analysis of images: Inst. Comput. Sci. Appl. Math., Christian-Albrechts-Univ. Kiel, Kiel, Germany.

Ell, T., 1992, Hypercomplex spectral transformations: PhD thesis, Univ. Minnesota.

Hamilton, W., 1866, Elements of quaternions: Longmans Green, London.

Lumley, D., 1995, Seismic time-lapse monitoring of subsurface fluid flow: PhD thesis, Stanford University.

Sanwine, S. and T. Ell, 2000, Colour image filters based on hypercomplex convolution: Colour image filters based on hypercomplex convolution:, IEEE Proceedings- Vision, Image and Signal Processing, 89–93.

Tang, Y. and R. G. Clapp, 2006, Lloyd's algorithm for selecting reference anisotropic parameters during wavefield extrapolation: 76th Ann. Internat. Mtg., Soc. of Expl. Geophys.